

Fe I in the β Pictoris circumstellar gas disk

I. Physical properties of the neutral iron gas

A. Vidal-Madjar^{1,2}, F. Kiefer^{1,2,3}, A. Lecavelier des Etangs^{1,2}, V. Bourrier⁴, D. Ehrenreich⁴, R. Ferlet^{1,2},
G. Hébrard^{1,2}, and P. A. Wilson^{1,2}

¹ CNRS, UMR 7095, Institut d'Astrophysique de Paris, 98^{bis} boulevard Arago, F-75014 Paris, France

² UPMC Univ. Paris 6, UMR 7095, Institut d'Astrophysique de Paris, 98^{bis} boulevard Arago, F-75014 Paris, France

³ School of Physics and Astronomy, Tel-Aviv University, Tel-Aviv 69978, Israel

⁴ Observatoire de l'Université de Genève, 51 chemin des Maillettes, 1290, Sauverny, Switzerland

ABSTRACT

The young planetary system β Pictoris is surrounded by a circumstellar disk of dust and gas. Because both dust and gas have a lifetime shorter than the system age, they need to be replenished continuously. The gas composition is partly known, but its location and its origin are still a puzzle. The gas source could be the exocomets (or so-called falling and evaporating bodies, FEBs), which are observed as transient features in absorption lines of refractory elements (Mg, Ca, and Fe) when they transit in front of the star at several tens of stellar radii.

Nearly 1700 high-resolution spectra of β Pictoris have been obtained from 2003 to 2015 using the HARPS spectrograph. In these spectra, the circumstellar disk is always detected as a stable component among the numerous variable absorption signatures of transiting exocomets.

Summing all the 1700 spectra allowed us to reach a signal-to-noise ratio higher than 1000, which is an unprecedentedly high number for a β Pictoris spectrum. It revealed many weak Fe I absorption lines of the circumstellar gas in more than ten excited states. These weak lines bring new information on the physical properties of the neutral iron gas in the circumstellar disk. The population of the first excited levels follows a Boltzmann distribution with a slope consistent with a gas temperature of about 1300 K; this temperature corresponds to a distance to the star of $\sim 38 R_{\text{Star}}$ and implies a turbulence of $\xi \sim 0.8$ km/s.

Key words. Stars: planetary systems

1. Introduction

When its IR excess was detected by the IRAS satellite in 1983, β Pictoris (HD 39060; HR 2020) was the first star with a detection of a circumstellar disk that is seen edge-on (Smith & Terrile 1984). Direct or indirect evidence of dust, gas, and falling and orbiting evaporating bodies (FEBs and OEBs, see, *e.g.*, Lecavelier et al. 1996a; Lecavelier 1998) and even planets were obtained very early (see review by Vidal-Madjar et al. 1998).

Absorption spectroscopic studies have revealed a stable gas component at the stellar radial velocity (~ 20 km/s in the heliocentric reference frame) and variable absorptions that have been attributed to transiting exocomets. The gas composition is relatively well constrained (Roberge et al. 2000). Emission line imaging also confirmed the presence of gas in the form of mainly Na I, Ca II, and Fe I (Brandeker et al. 2004).

All these spectroscopic studies concluded that although the gas should be ejected away from the system by radiation pressure, it is observed in Keplerian rotation. Lagrange et al. (1998) proposed that atomic hydrogen could act as a braking gas at about 0.5 AU. Brandeker et al. (2004) observed different species in emission, and in particular, Ca II, Na I, and Fe I, which confirmed the braking gas scenario. Fernández et al. (2006) later proposed that atomic

carbon (mostly ionized) could be the required braking gas. C II, which is overabundant by more than ten times solar (Roberge et al. 2006), could very efficiently brake all species via Coulomb interaction simply because carbon suffers very little radiation pressure. This was also confirmed more recently by Brandeker (2011), who observed the Fe I and Na I lines in absorption and showed that the shift between the two sets of lines could also be explained by an overabundant C II braking gas.

However, the source of all the observed species within the so-called stable gas disk has yet to be found. It is clear that the FEBs are expelling gas, but it is not obvious that the gas observed in emission in the disk (*e.g.*, Brandeker et al. 2004) necessarily comes from the FEBs. In particular, the C gas may be coming from dissociated CO released far from the star (Vidal-Madjar et al. 1994; Jolly et al. 1998). From the CO evaluated temperature, ~ 20 K, a distance of about 100 AU was estimated, allowing Lecavelier et al. (1996, 1998) to hypothesize that a second source could be related to distant OEBs. This was clearly confirmed by the recent CO detection with ALMA (Dent et al. 2014; Matrà et al. 2017) at about 80 AU from the star. All species origins could thus also be related to the accretion from this 80 AU “birth ring”. However, metals and C could have different origins. If for metals the gas source is close to the central star, radiation pressure could push the gas at large distances where it is also observed. In this frame, the ex-

Send offprint requests to: A.V.M. (e-mail: alfred@iap.fr)

ocometes (or FEBs) could also be the source of the stable metal species that are present in the circumstellar disk. The nature and properties of these infalling comets were constrained by observations and models (Ferlet et al. 1987; Beust et al. 1989, 1990; Beust & Valiron 2007). More recently, detailed studies showed that these exocomets are distributed into two dynamical families (Kiefer et al. 2014).

Our understanding of detailed mechanisms acting now in the young β Pictoris planetary system could help us to reconstruct the puzzle of early phases in the young solar system. The late heavy bombardment, for instance, could have played an important role in the evolution of the Earth atmosphere. Interaction with the central star, nearby interstellar clouds, supernova events, and cometary bombardments have built up an evolved Earth atmosphere and brought our oceans, where finally life appeared (see, *e.g.* *Central star*: Sekiya, Nakazawa & Hayashi 1980; Watson, Donahue & Walker 1981; Kasting & Pollack 1983; Hunten, Pepin & Walker 1987. *Interstellar clouds*: Hoyle & Lyttleton 1939; McCrea 1975; Begelman & Rees 1976; Talbot & Newman 1977; Vidal-Madjar et al. 1978; Lallement et al. 2003; Gry & Jenkins 2014. *Supernovae*: Rubenstein et al 1983; Trimble 1983; Li 2008. *Comets*: Rampino & Stothers 1984; Morbidelli et al. 2000; Teiser & Wurm 2009. *Cosmic-rays*: Laviolette 1987. *System formation*: Zahnle, Kasting & Pollack 1988; Pepin 1991; Raymond, Quinn & Lunine 2004; Genda & Ikoma 2007; Kral et al. 2016. *Life*: Pavlov & Klabunovskii 2015).

More than 1700 high-resolution spectra of β Pictoris were obtained with the HARPS spectrograph. Stacking all these spectra into one, the total signal-to-noise ratio (S/N) was higher than 1000 at shorter wavelengths and even 2000 at longer wavelengths. This high-resolution high-S/N spectrum revealed numerous newly detected weak absorption lines of the β Pictoris circumstellar Fe I gas.

Most importantly, the majority of these absorption features correspond to transition lines from initial excited states of neutral iron. Characterizing the distribution of the states of circumstellar Fe I can help to constrain the physical properties of the Fe I gas in the disk of β Pictoris, under the influence of the stellar radiation.

In this paper we first present the observations (Sect. 2). The measurements of the physical properties of the gas for various excitation levels of Fe I are given in Sect. 3. The results are discussed in Sect. 4.

2. Observations

The β Pictoris system has been monitored with the HARPS spectrograph mounted on the 3.6m telescope of La Silla (ESO Chile) from 2003 to 2015 on a (mostly) regular basis (except between 2004 and 2007 and in 2012). The spectra were primarily obtained to constrain the mass of planets around β Pictoris using radial velocity measurements (Lagrange et al. 2012) and to analyze the statistics of the exocomets (Kiefer et al. 2014). Since β Pictoris is observable only during the summer in the southern hemisphere, the observations were carried out essentially from September to April of each season. The 1D spectra were extracted via the standard most recent HARPS pipeline (DRS 3.5), including localization of the spectral orders in the 2D images, optimal order extraction, cosmic-ray rejection, wavelength calibration, flat-field corrections, and 1D reconnection of

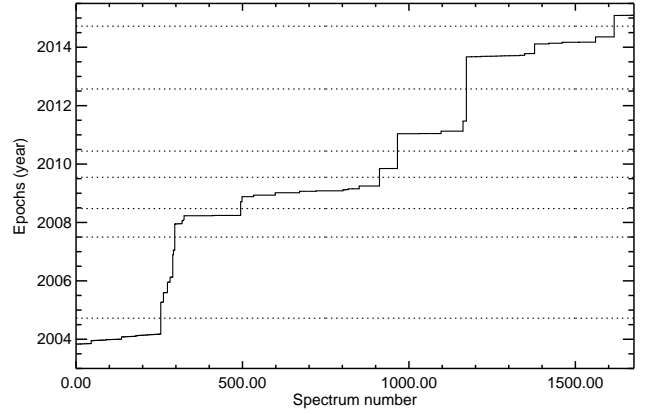


Fig. 1. Time distribution of the HARPS observing nights used in our study. The horizontal dotted lines show the limits of various observation campaigns.

Table 1. Repartition of HARPS observations. The S/N is calculated next to the main Fe I line between 3859.30 Å and 3859.70 Å.

Periods (year)	N_{obs}	Total S/N at 3860 Å	Average Epoch (year)
2003-2004	255	962	2004.025
2004-2007	42	390	2006.235
2007-2008	198	492	2008.203
2008-2009	417	909	2009.070
2009-2010	54	278	2009.847
2010-2011	207	467	2011.081
2013-2014	453	799	2013.929
2014-2015	60	493	2015.091

the spectral orders after correction for the blaze. We organized the spectra into different samples, each constituting one summer of observations, with the exception of the period 2004-2007. During this period, the average number of spectra observed per summer is 14, which is very small compared to the other period averages (234 spectra per summer). For this reason, we created a special sample covering the three summers from 2004 to 2007. This repartition is summarized in Table 1 and Fig. 1.

The 1D spectra of each period are all summed, weighting each spectrum F_i with its square of the $(S/N)_i$ at order 33 (with a median wavelength of 4745.55 Å). This order was selected because of its proximity to the median HARPS order while being as flat as possible and not affected by any broad stellar line or telluric signature. The following formula was used to derive the summed spectra:

$$F_{\text{sum}} = \frac{\sum_{i=1}^{N_{\text{spec}}} F_i \times (S/N)_i^2}{\sum_{i=1}^{N_{\text{spec}}} (S/N)_i^2}, \quad (1)$$

where N_{spec} is the total number of spectra F_i , and $(S/N)_i$ is the signal-to-noise ratio of each spectrum i .

In the spectra coaddition, no resampling was needed thanks to the high stability of the spectrograph and the HARPS data reduction software (DRS), which produces the spectra on the same wavelength scale for all spectra in the solar system barycentric reference frame¹. We checked

¹ eso.org/sci/facilities/lasilla/instruments/harps/doc/DRS.pdf

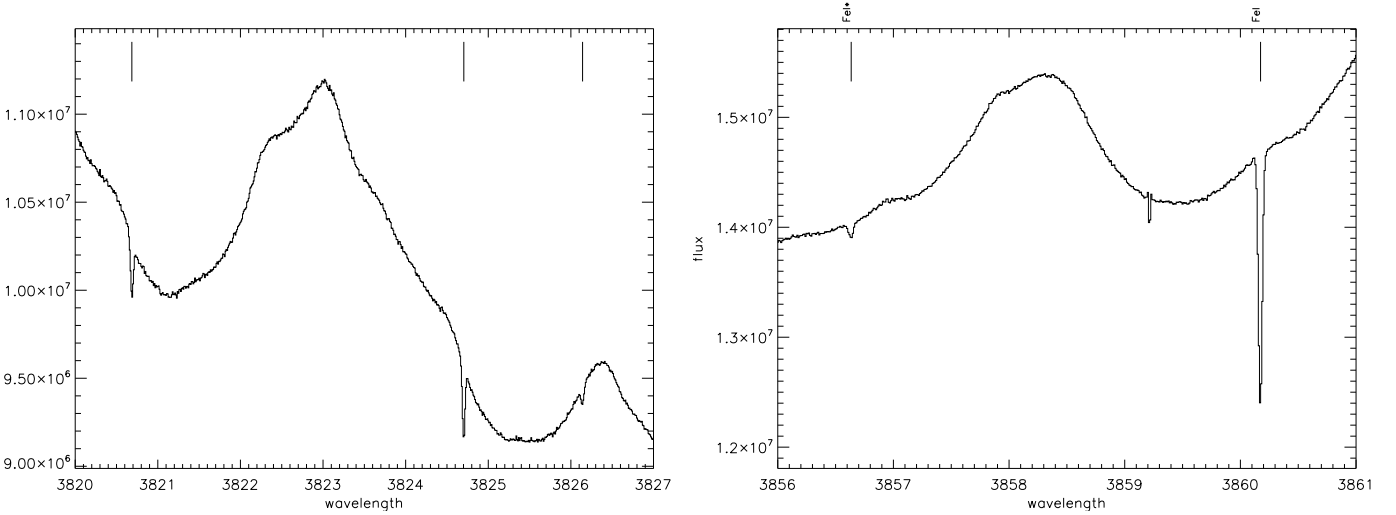


Fig. 2. Averaged HARPS spectra of β Pictoris (flux as a function of wavelength in Å). They reveal the very high S/N ratio achieved, even at very short wavelengths at 3820 Å and 3860 Å. Each detected FeI line is indicated by a tick mark at +20.5 km/s, *i.e.*, the β Pictoris heliocentric radial velocity. The detected signatures are due to the stable gas within the circumstellar disk.

Left: Section of the spectrum from 3820 to 3827 Å. Three lines are detected: one line from the 6928 cm^{-1} excited levels at 3820.7 Å, one line from the ground base level near 3824.7 Å, and one line from the 7377 cm^{-1} excited levels at 3823.15 Å. **Right:** Spectral region from 3856 to 3861 Å. The strongest FeI line from ground base level is seen near 3860.15 Å, as well as the line from the 416 cm^{-1} excited level (noted FeI* near 3856.65 Å).

that the zero flux level of the 1D spectra was always well defined. To this purpose, we considered the tip of the Ca II circumstellar (CS) absorption line, which should be zero. We found that 122 of 1686 spectra have a negative flux at the tip of the Ca II CS line at about -10 ADU, which is negligible with respect to the typical flux around the FeI lines, of about 10^4 ADU. Moreover, the S/Ns of these 122 spectra are among the lowest in the full sample.

Coadding the spectra greatly improved the S/N of β Pictoris spectrum in each period. We give in Table 1 the value of the S/N around the main Fe I CS line at 3860 Å. We calculated it by fitting the flux continuum by a second-degree polynomial between 3859.30 Å and 3859.70 Å, a rather flat region next to the Fe I CS line. We estimated the noise from the standard deviation of the residuals and the signal from the average flux.

Because the stable gas is continuously present in the β Pictoris spectra, all possible remaining variable spectral features are washed away in the stacking process. We ran the procedure defined in the Kiefer et al. (2014) to recover the β Pictoris reference spectrum with no variable absorptions by searching for the highest flux over each pixel at each wavelength. This approach was necessary in the case of the CaII lines, where almost every spectrum includes an exocomet transit event. Here we checked the possible pollution of the strongest FeI absorption lines by exocomet transits using this procedure. We found that the line profiles obtained using this process were identical to the profile obtained using a simple coaddition process, showing that the pollution by FEB signatures is negligible. A few FEBs were observed in Fe I (Welsh & Montgomery 2015, 2016); there is, however, a very low number of detections, and all of them are found to be at high radial velocity, away from the stable gas absorption signature, which remains at the

stellar radial velocity. The pollution of the FeI profile by transiting exocomets is therefore negligible.

Finally, we stacked all gathered spectra and averaged them in order to improve the S/N. Given the high stability of the spectrograph, the spectral resolution is not degraded ($R \sim 115000$; Mayor et al. 2003) after the stacking and averaging process. This resolving power was furthermore independently confirmed by Brandeker (2014), who found that in HARPS observations common to ours, the resolving power was on the order of 112000. The result is spectacular, as shown in Figure 2. The S/N reached is on the order of 1000 at the shorter wavelengths and up to 2000 at longer wavelengths of the HARPS spectrum.

3. Stable gas in β Pictoris

Because of the very high S/N ratio achieved, we are able to detect numerous FeI lines in the ground state as well as in several excited levels. All the detected FeI lines are listed in Table 2.

The profiles of the the strongest lines of the 12 FeI excited levels that we detected are shown in Fig. 4. Lines from excited levels up to 12969 cm^{-1} are clearly detected. Several absorption lines of highly excited levels have a low column density, but they lie in spectral regions above 4000 Å, where the high flux level yields a high S/N, which allows sensitive detections and accurate measurement of column densities.

3.1. Circumstellar gas in the ground base FeI lines

We used the profile-fitting procedure `Owens.f`, developed by Lemoine M. and the FUSE French Team (see *e.g.* Lemoine et al. 2002; Hébrard et al. 2002) for the analy-

Table 2. FeI lines (i lower level, k upper level). The equivalent widths given in the last column are derived from the column densities measured in Sect.3.1, which are listed in Table 6.

FeI lines (Å)	A_{ki} (s^{-1})	f_{ik}	E_i (cm^{-1})	E_k (cm^{-1})	W_{eq} (mÅ)
3795.002	1.15×10^7	3.47×10^{-2}	7986	34329	0.047
3799.547	7.31×10^6	2.04×10^{-2}	7728	34040	0.019
3812.964	7.91×10^6	1.23×10^{-2}	7728	33947	0.011
3815.840	1.12×10^8	1.90×10^{-1}	11976	38175	0.115
3820.425	6.67×10^7	1.20×10^{-1}	6928	33096	1.269
3824.443	2.83×10^6	4.83×10^{-3}	0	26140	1.569
3825.881	5.97×10^7	1.02×10^{-1}	7377	33507	0.400
3827.822	1.05×10^8	1.65×10^{-1}	12561	38678	0.044
3834.222	4.52×10^7	7.13×10^{-2}	7728	33802	0.067
3840.437	4.70×10^7	6.24×10^{-2}	7986	34017	0.086
3841.047	1.36×10^8	1.80×10^{-1}	12969	38996	0.030
3849.966	6.05×10^7	4.49×10^{-2}	8155	34122	0.027
3856.371	4.64×10^6	7.39×10^{-3}	416	26340	0.382
3859.911	9.69×10^6	2.17×10^{-2}	0	25900	7.182
3865.523	1.55×10^7	3.47×10^{-2}	8155	34017	0.021
3878.573	6.17×10^6	8.36×10^{-3}	704	26479	0.245
3886.282	5.29×10^6	1.20×10^{-2}	416	26140	0.630
3895.656	9.39×10^6	7.13×10^{-3}	888	26550	0.082
3899.707	2.58×10^6	5.89×10^{-3}	704	26340	0.174
3906.479	8.32×10^5	1.90×10^{-3}	888	26479	0.022
3920.257	2.60×10^6	1.79×10^{-2}	978	26479	0.072
3922.911	1.08×10^6	3.19×10^{-3}	416	25900	0.171
3927.919	2.60×10^6	1.00×10^{-2}	888	26340	0.117
3930.296	1.99×10^6	6.46×10^{-3}	704	26140	0.194
4045.812	8.62×10^7	2.12×10^{-1}	11976	36686	0.144
4063.594	6.65×10^7	1.65×10^{-1}	12561	37163	0.049
4071.738	7.64×10^7	1.90×10^{-1}	12969	37521	0.036
4271.760	2.28×10^7	7.62×10^{-2}	11976	35379	0.058
4307.902	3.38×10^7	1.21×10^{-1}	12561	35768	0.041
4325.762	5.16×10^7	2.03×10^{-1}	12969	36079	0.043
4383.544	5.00×10^7	1.76×10^{-1}	11976	34782	0.140
4404.750	2.75×10^7	1.03×10^{-1}	12561	35257	0.036

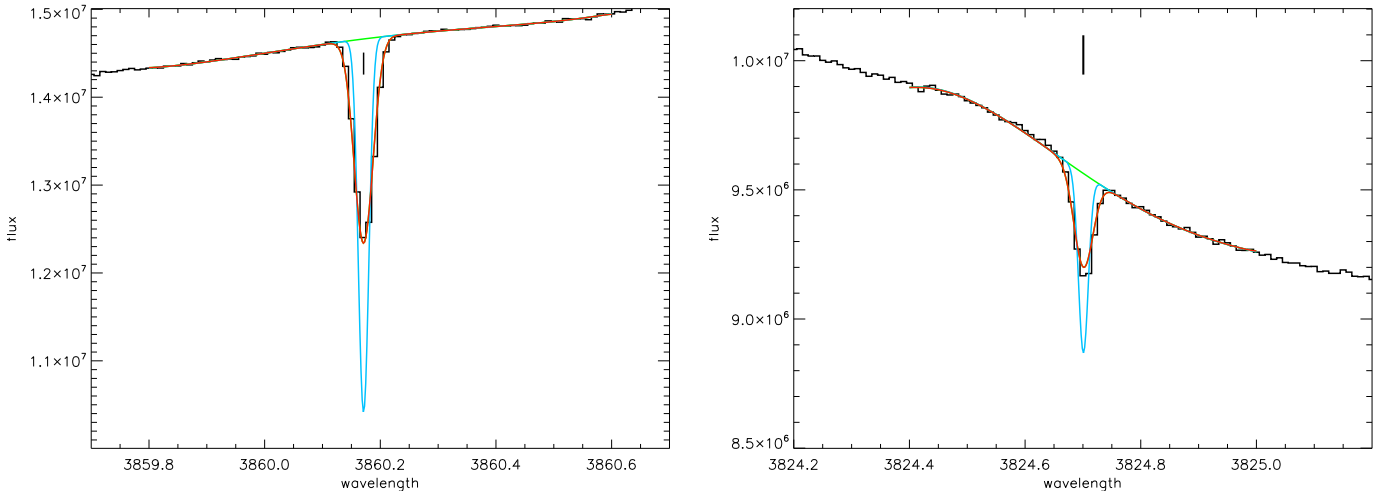


Fig. 3. Two FeI β Pictoris lines from the ground base level (flux in arbitrary units as a function of wavelength in Å). The observations are shown as black histograms, the fitted stellar continuum as green lines. The blue lines represent the intrinsic absorption feature, and the red lines are its convolution with the HARPS instrumental profile. In the two lines, the intrinsic absorption profiles (blue lines) are far from saturated, implying that the column density of FeI from the ground base level can be well constrained.

Table 3. Fe I excitation levels corresponding to the detected absorption lines. The lower levels of the 12 excited levels range from 416 to 12969 cm^{-1} .

Energy level (cm^{-1})	Energy level (K)	J	Number of lines
0	0	4	2
416	598	3	3
704	1013	2	3
888	1278	1	3
978	1407	0	1
6928	9968	5	1
7377	10614	4	1
7728	11120	3	3
7986	11490	2	2
8155	11733	1	2
11976	17232	4	4
12561	18073	3	4
12969	18660	2	3

sis. The absorption lines were fit by Voigt profiles using χ^2 minimization. Using `Owens.f`, we searched for the best simultaneous fit to all detected spectral lines assuming that all line profiles are the result of absorption by a low number of components with, for a given component, the same values for the radial velocity, V , the temperature, T , the turbulent broadening, ξ , and the column densities for each species s , N_s . The width of the lines, b , results from both parameters T and ξ , with $b^2 = (2kT/m)^2 + \xi^2$ (where k is the Boltzmann constant and m is the mass of the considered species). The degeneracy in the measurement of T and ξ can be left only when several species with different masses are fit simultaneously, which is not the case here because we considered only the iron absorption features. We emphasize that the column densities and their associated error bars were derived from a global fit of the lines profiles and not from the equivalent width measurements. The equivalent widths listed in Table 2 are given for comparison purposes.

In a first step, a single component was considered to fit the two observed Fe I lines from the ground base level. The stellar continuum was modeled by a fourth-order polynomial, and the absorption profile by the convolution of the instrument line spread function (LSF) with a Voigt profile defined by its standard parameters (V , b , and N). The fitted profiles are shown in Fig. 3, and the corresponding parameters are listed in Table 4.

The line width (b) is on the order of 0.8 km/s, which is very narrow (the HARPS instrumental width is 2.6 km/s) and in contrast with all published b values for the β Pictoris stable circumstellar component measured using the complex Ca II doublet, which are all on the order of 2 km/s. We interpret this low value of b as the combination of two factors: 1) iron has a higher mass than calcium, leading to a lower line width in its thermal component, 2) the Fe I line is less complex, with no stellar chromospheric emission variations and no significant pollution by variable exocomet absorption events. As a result, the line width measured here is likely closer to the real physical value. This narrow line width furthermore shows that the stacking process of hundreds of HARPS spectra does not significantly affect the line profile (in agreement with the expected stability for the HARPS spectrograph).

To evaluate the error bars on the parameter estimates, we calculated the $\Delta\chi^2$ variations resulting from the change

Table 4. Measurements for the Fe I ground base level obtained with a simultaneous fit of the profiles of the two lines.

V_{FeI}	b_{FeI}	N_{FeI}
Heliocentric radial velocity (km/s)	Line width (km/s)	Column density ($\times 10^{13} \text{ cm}^{-2}$)
20.19 ± 0.05	0.80 ± 0.07	$0.251 (\pm 0.01)$

Table 5. Same as Table 4 for the two Fe I* and one Fe I** lines

$V_{\text{FeI*}, \text{FeI**}}$	$b_{\text{FeI*}, \text{FeI**}}$	$N_{\text{FeI*}}$	$N_{\text{FeI**}}$
(km/s)	(km/s)	($\times 10^{12} \text{ cm}^{-2}$)	($\times 10^{12} \text{ cm}^{-2}$)
20.50 ± 0.10	1.25 ± 0.38	0.46 ± 0.04	0.25 ± 0.05

of the tested parameters, while other parameters were let free to vary (see Hébrard et al. 2002). The resulting error bars for the Fe I radial velocity V_{FeI} , line width b_{FeI} , and column density N_{FeI} are given in Table 4.

The estimated column density of Fe I is robust because the two lines are unsaturated and the resulting equivalent width is in the linear part of the curve of growth; the estimate is thus independent of the velocity distribution of the absorbing gas. This column density corresponds to an equivalent width of 7.1 mÅ for the 3860 Å line, which is consistent with the equivalent width measured by Welsh & Montgomery (2016). The variations in column density detected by Welsh & Montgomery (2016) do not affect the scientific conclusions derived here and will be discussed in a forthcoming paper (Kiefer et al., in preparation).

3.2. Circumstellar gas in the Fe I excited lines

3.2.1. Fe I* and Fe I** lines

Following the same process as in Sect. 3.1, we analyzed the three strong lines from the two first excited levels at 416 cm^{-1} (noted Fe I* at 3856.371 and 3886.282 Å) and 704 cm^{-1} (noted Fe I** at 3878.573 Å). The results are presented in Table 5.

We found that each of these three lines is at the same radial velocity of 20.50 km/s. This velocity is significantly higher than the radial velocity measured for the Fe I line from the ground base level, $V_{\text{FeI}} = 20.19 \text{ km/s}$. It also appears that the widths of the line for excited levels seem to be larger than those of the lines from ground base level, but the difference is barely significant.

3.2.2. All the Fe I lines from excited levels

Here we assumed that all the detected absorptions in Fe I lines from excited levels arise from a single medium. We thus used only a single absorption component to fit the profiles of all Fe I lines from the excited levels listed in Table 2. The fits of the strongest lines of each excited level are shown in the Fig. 4, excluding the lines from the 7728 cm^{-1} , 7986 cm^{-1} , and 8155 cm^{-1} excited levels because they are too weak to be visible in such a plot.

Using a simultaneous fit to all the identified Fe I lines from excited levels, we found

$$V_{\text{Exc}} = 20.41^{+0.03}_{-0.05} \text{ km/s},$$

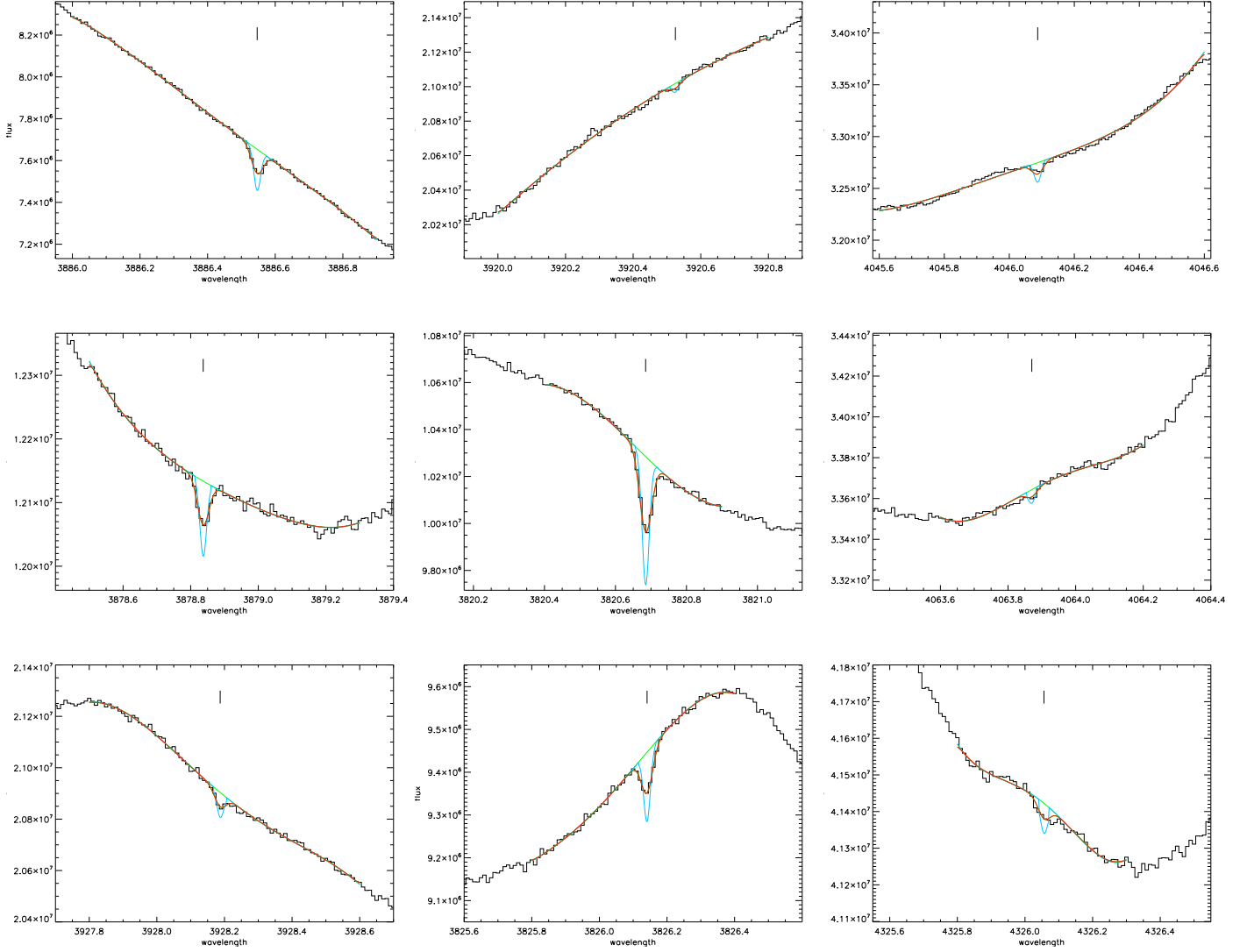


Fig. 4. Simultaneous fits of the strongest FeI lines from excited levels. **First column:** The 416 cm^{-1} , 704 cm^{-1} and 888 cm^{-1} excited levels (from top to bottom). **Second column:** The 978 cm^{-1} , 6928 cm^{-1} and 7377 cm^{-1} excited levels (from top to bottom). **Third column:** The 11976 cm^{-1} , 12561 cm^{-1} and 12969 cm^{-1} excited levels (from top to bottom). The stellar continuum is plotted with a green line, the intrinsic absorption profile with a blue line, and the absorption profile convolved with the HARPS instrument profile with a red line. The gas responsible for the absorption lines is defined as a unique component with the same radial velocity and line width (b value) for all the excited levels; the column densities of each excited level are independent. The positions of the absorption lines are indicated by a tick at $+20.41\text{ km/s}$ radial velocity.

$$b_{\text{Exc}} = 1.01 \pm 0.06\text{ km/s}.$$

The width of the lines is found to be narrow with $b \sim 1\text{ km/s}$. This strengthens the hypothesis that the entire absorption from the excited levels arises from a single component within the same circumstellar medium at the same radial velocity. When we acknowledge that a fraction of the line widths is due to thermal broadening, the measured b value provides an estimate for the maximum temperature of the gas, which is given by $T_{\text{Exc}}^{\text{Max}} = b_{\text{Exc}}^2 * m_{\text{Fe}} / (2k)$. We find $T_{\text{Exc}}^{\text{Max}} < 3700 \pm 400\text{ K}$.

The measured column densities of the 12 FeI excited levels are given in Table 6. For ten of the listed excited levels, the signatures are detected at more than 3σ . For the

levels from 7728 cm^{-1} and from 8155 cm^{-1} , the detections are at a significance lower than 2σ , and the corresponding column densities can be considered as upper limits. The measured column densities cover more than two orders of magnitude.

3.3. Two-component FeI ground base level

The measured radial velocity of the gas component producing the absorption in all these excited FeI lines, $V_{\text{Exc}} = 20.41^{+0.03}_{-0.05}\text{ km/s}$, is different at 4σ from the radial velocity measured in the two FeI lines from the ground base level, $V_{\text{FeI}} = 20.19 \pm 0.05\text{ km/s}$. Nonetheless, the gas observed in the excited levels must also include a population of FeI

Table 6. Column densities of the 12 excited levels of the FeI lines. σ represents the significance of the detection.

Excited level (cm^{-1})	N (cm^{-2})	Error (+/-) (cm^{-2})	σ
416	0.393×10^{12}	$(+0.011/-0.011) \times 10^{12}$	36.
704	0.220×10^{12}	$(+0.010/-0.010) \times 10^{12}$	22.
888	0.857×10^{11}	$(+0.081/-0.079) \times 10^{11}$	11.
978	0.296×10^{11}	$(+0.099/-0.080) \times 10^{11}$	3.0
6928	0.819×10^{11}	$(+0.021/-0.019) \times 10^{11}$	41.
7377	0.303×10^{11}	$(+0.016/-0.015) \times 10^{11}$	20.
7728	0.720×10^{10}	$(+0.400/-0.390) \times 10^{10}$	1.8
7986	0.106×10^{11}	$(+0.025/-0.026) \times 10^{11}$	4.2
8155	0.451×10^{10}	$(+0.270/-0.270) \times 10^{10}$	1.7
11976	0.469×10^{10}	$(+0.049/-0.052) \times 10^{10}$	9.2
12561	0.205×10^{10}	$(+0.055/-0.011) \times 10^{10}$	19.
12969	0.129×10^{10}	$(+0.019/-0.023) \times 10^{10}$	5.6

atoms at the ground base level. Therefore the measured difference in radial velocity supports the idea that the absorptions in the FeI lines from the ground base level can have two components: one at the same radial velocity as the absorption from the excited levels, and a second component at a lower radial velocity.

We therefore fit the profile of the FeI lines from ground base level with two components: a redward component (1) using the same radial velocity as the velocity found for the absorptions from all excited levels, and a blueward component (2) with a radial velocity let free to vary in the fitting procedure (Fig. 5) The results are the following:

$$\begin{aligned}
 V_{\text{FeI}}^1 &= 20.41 \text{ km/s (fixed),} \\
 b_{\text{FeI}}^1 &= 1.01 \text{ km/s (fixed),} \\
 N_{\text{FeI}}^1 &= (0.956^{+0.002}_{-0.059}) \times 10^{12} \text{ cm}^{-2}, \\
 V_{\text{FeI}}^2 &= 20.07^{+0.02}_{-0.01} \text{ km/s,} \\
 b_{\text{FeI}}^2 &= 0.59^{+0.04}_{-0.01} \text{ km/s,} \\
 N_{\text{FeI}}^2 &= (1.57^{+0.06}_{-0.01}) \times 10^{12} \text{ cm}^{-2}, \\
 N_{\text{FeI}}^{\text{Total}} &= (2.53^{+0.06}_{-0.07}) \times 10^{12} \text{ cm}^{-2}, \\
 \Delta V &= 0.34^{+0.04}_{-0.05} \text{ km/s.}
 \end{aligned}$$

The velocities of the two components V_{FeI}^1 and V_{FeI}^2 are found to be significantly different. The highest column density in FeI is found to be in the second component (2).

The presence of two components is supported by the goodness-of-fit improvement when using the two-components model. With the addition of a second component, the χ^2 decreases from 120.3 (with 139 degrees of freedom) to 114.9 (with 138 degrees of freedom). The Akaike information criterion (AIC) decreases by 3.4 with the second model, which shows that the presence of a second component is definitely favored (the BIC is also lower).

When V^1 and b^1 were left free to vary in the fit, the χ^2 decreases only to 112 with similar values for all parameters, despite the two new degrees of freedom. This confirms that the detected second component in the FeI ground base level is likely the expected counterpart of the absorption seen in the excited levels, with the same physical properties (V and b) for both excited and ground base levels.

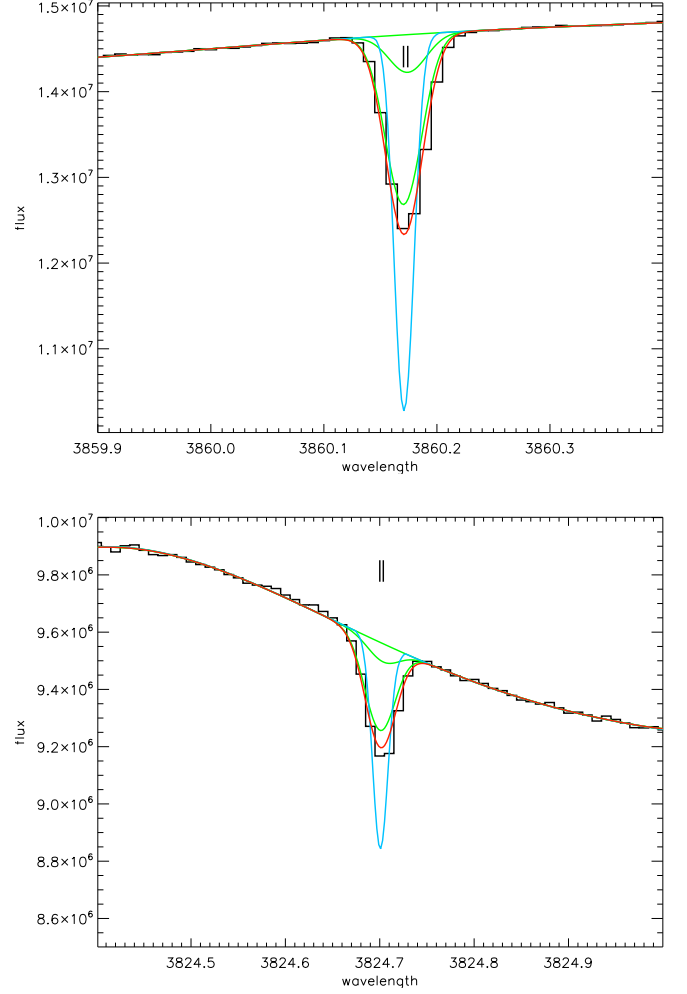


Fig. 5. Same as Fig. 3 with two-component fits to the line absorption profiles. The positions of the two components are shown by two small vertical tick marks. The absorption profiles of each of the two components are shown by green lines. The redward component (1) is at the same radial velocity as the absorption from all excited levels. The blueward component (2) has a higher column density, but is detected only in the FeI lines from the ground base level.

4. Discussion

4.1. FeI excited levels

The FeI excited levels can be populated either by radiation or by collisions if the medium is dense enough. Therefore, the FeI excited levels signatures are not observed in the interstellar medium (ISM) absorption lines because the volume density of the ISM in the vicinity of the Sun and the exciting photon flux are too low. The FeI ground base level lines are also not usually observed in the ISM for another reason: iron atoms are easily ionized in the ISM UV flux. As a result, all the FeI lines detected here arise from the circumstellar medium of β Pictoris.

In an excitation diagram $[E_K, \log_{10}(N/g)]$ where for each considered excited level, E_K is the level energy expressed in Kelvin, N the column density and g the g-factor ($g=2J+1$, see Table 3), the population of the excited lev-

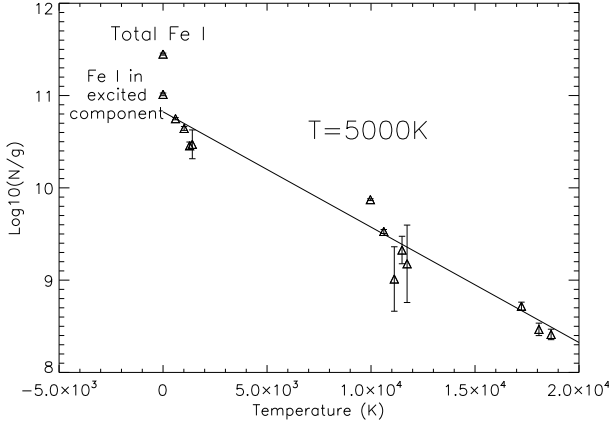


Fig. 6. Excitation diagram of the level populations with $\log_{10}(N/g)$ as a function of the level energy in Kelvin with 1σ error bars. The least-squares fit is shown as a straight solid line and corresponds to a 5000 K thermodynamic equilibrium distribution. The disagreement between this line and the observations shows that the observations do not correspond to LTE conditions.

Table 7. Sensitivity to the stellar flux of the different excited levels, as shown by the sum of the oscillator strengths of their lines, below or above the Balmer discontinuity (at about 3700\AA), b BD or a BD, respectively. N_{bBD} and N_{aBD} are the numbers of lines for each category, and Σ_{bBDF} and Σ_{aBDF} are the sums of the oscillator strengths.

E_i (cm^{-1})	N_{bBD}	Σ_{bBDF}	N_{aBD}	Σ_{aBDF}	$\Sigma_{bBDF} / \Sigma_{aBDF}$
0	22	1.3964	3	0.06763	20.65
416	29	1.3245	5	0.06730	19.68
704	33	1.3860	5	0.06491	21.35
888	29	1.4609	4	0.06273	23.29
978	14	1.5324	2	0.06410	23.91
6928	27	0.63980	3	0.31334	2.042
7377	34	0.65591	6	0.30843	2.127
7728	36	0.68351	7	0.29204	2.340
7986	32	0.65986	8	0.27952	2.361
8155	25	0.68376	6	0.26621	2.568
11976	9	0.04452	8	0.73459	0.0606
12561	13	0.04715	10	0.72093	0.0654
12969	10	0.04980	8	0.73392	0.0679

els at local thermodynamic equilibrium (LTE) follow a linear relationship whose slope is linked to the temperature of the medium. This diagram is shown in Fig. 6 for the Fe I excited level column density evaluations. Their distribution is not linear, showing that LTE conditions are not met in the considered medium where the Fe I lines are observed. The least-squares linear fit is shown. It corresponds to a temperature of about 5000 K, quite different from the effective temperature of the β Pictoris photosphere ($T_{eff} \sim 8000\text{ K}$). This shows that the populations of the different levels are not only controlled by radiation, but also by collisions. This argues for an equilibrium that is neither radiative nor collisional, but somewhere in between radiative and collisional regimes, as described for instance by Viotti (1976; see Sect. 4.2.2).

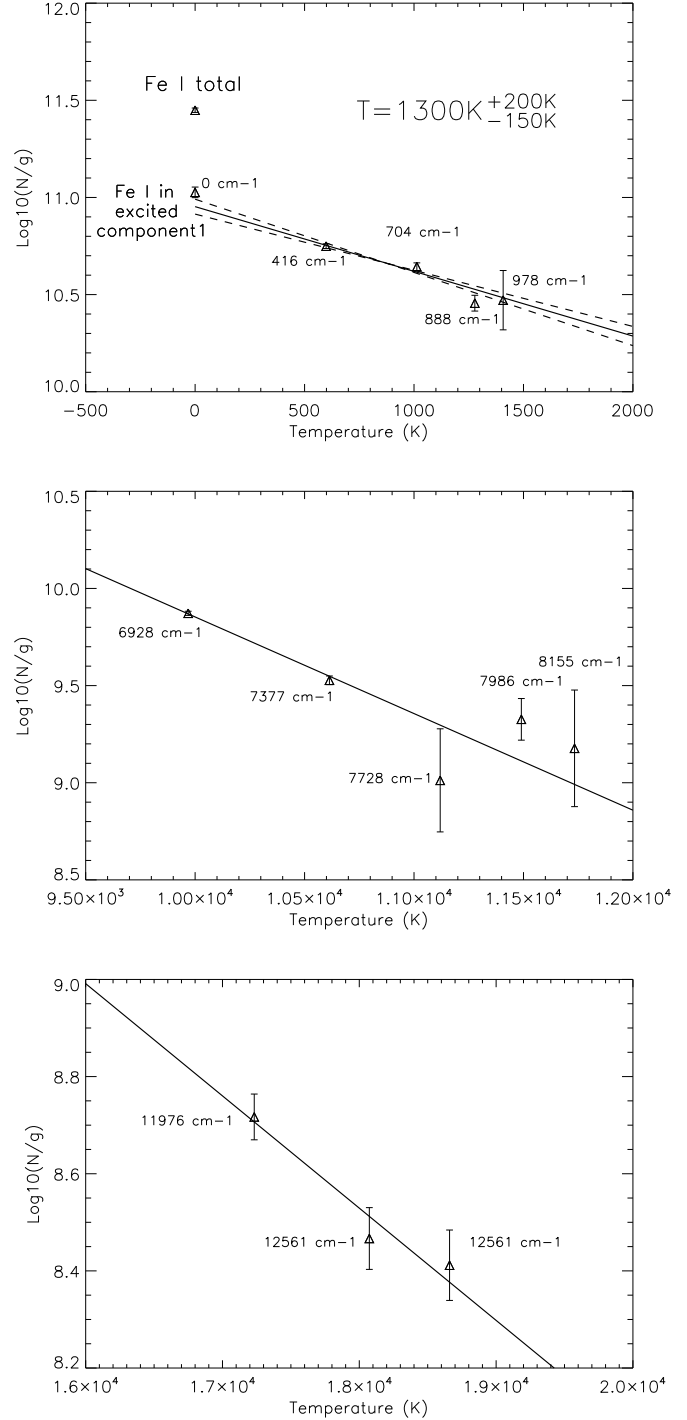


Fig. 7. Same as Fig. 6, but in three separate plots corresponding to the three domains. **Top:** Low-energy levels. **Middle:** Medium-energy levels. **Bottom:** High-energy levels. Least-squares fits of all available levels are shown as solid straight lines. For the low energy levels, the 0 cm^{-1} level corresponding to component 1 is not included in the fit (see text). Limits on the least-squares slope are shown as dashed lines for the low-energy levels, centered over the weighted average of the four excited levels. The population of the low-energy levels follow a Boltzmann distribution, which is consistent with an excitation temperature of about 1300 K.

In the energy diagram (Fig. 6), the energy levels are clustered within three groups. We recall that the slope corresponding to 8000 K equilibrium conditions should be smaller than the slope of the 5000 K conditions, therefore the lower energy level column densities are relatively too high, while the higher energy levels are relatively too low.

Because the β Pictoris spectrum is not a perfect 8000 K black body, this behavior can be explained qualitatively. The three groups of energy levels are supplied by atomic transitions that are distributed along the stellar spectrum. Strong flux reductions, such as the deep Balmer lines and the Balmer discontinuity (BD) of an A5 spectrum below 3700 Å, will effectively underpopulate certain energy levels. For each energy level, we calculated the sum of all the oscillator strengths (with $f > 10^{-3}$) of all lines between 2000 Å and 9000 Å (where most of the Fe I lines occur). The number of lines counted below (N_{bBD}) and above (N_{aBD}) the Balmer discontinuity, as well as the sum of their oscillators strengths, $\Sigma_{bBD}f$ and $\Sigma_{aBD}f$, are given in Table 7. The ratio $\Sigma_{bBD}f / \Sigma_{aBD}f$, which represents the sensitivity of the considered level to the stellar flux, is also listed. These ratios are significantly different in the three groups of energy levels: ~ 20 for $E_i < 1000 \text{ cm}^{-1}$, ~ 2 for $6000 \text{ cm}^{-1} < E_i < 9000 \text{ cm}^{-1}$, and ~ 0.06 for $E_i > 11000 \text{ cm}^{-1}$. In these three domains, the radiative contribution is expected to be very different, as described below.

- 1) Group of High-energy levels above 11000 cm^{-1} . The highest energy levels have the highest photon-pumping efficiency because their spectroscopic lines lie higher than the Balmer discontinuity. For these levels, the radiative contribution is expected to be the dominant mechanism.
- 2) Group of Medium-energy levels, from 6000 cm^{-1} to 9000 cm^{-1} . For the levels in the group at intermediate energy, the photon-pumping efficiency has a medium value because the strongest lines of these levels are still present below the Balmer discontinuity. Here the radiative contribution should be less than for the higher energy levels.
- 3) Group of Low-energy levels, below 1000 cm^{-1} . The efficiency of the photon pumping in populating the low-energy levels is the lowest because their spectroscopic lines are mostly below the Balmer discontinuity. There the population of the levels by radiation is relatively less important and the dominant process could thus possibly be collisions.

The relative population of different energy levels can be analyzed within each group of energy levels: the group below 2000 K ($< 1000 \text{ cm}^{-1}$), the group around 11000 K (from 6000 cm^{-1} to 9000 cm^{-1}), and the group around 18000 K ($> 11000 \text{ cm}^{-1}$). The energy diagrams for each group are given in Fig. 7. It is noteworthy that the column density measured in component (1) of the ground base level is consistent with the column density extrapolated from the Boltzmann distribution in the energy diagram when we consider only the excited levels in the low-energy group (upper panel of Fig. 7), although they are one order of magnitude lower than the total Fe I column density. This strengthens the idea that component (1) in the ground base level is the counterpart of the gas detected in the excited levels.

From the alignment of the level populations, we can derive a characteristic temperature for the low-energy levels

of 1300^{+200}_{-150} K. Because the population in the low-energy levels is likely dominated by collisions, we can hypothesize that this temperature is a proxy for the measurement of the iron gas temperature. The b value of the same medium is evaluated to be $b_{\text{Exc}} = 1.01 \pm 0.06 \text{ km/s}$, which corresponds to a maximum temperature of $T_{\text{Exc}} < 3700 \pm 400 \text{ K}$. Assuming $T_{\text{Exc}} = 1300 \text{ K}$, we can derive the corresponding turbulent broadening ξ_{Exc} to be

$$\xi_{\text{Exc}} = 0.80 \pm 0.07 \text{ km/s}.$$

This new estimate of the turbulent broadening in the stable circumstellar gas yields a new constraint on any line width, which must be larger than $\sim 0.8 \text{ km/s}$, for any species. Of course, this constraint applies only where collisional equilibrium is reached and does not apply, for instance, in component (2) of Fe I described above, for which we found $b \sim 0.6 \text{ km/s}$ (see Section 3.3). In this last case, the broadening is likely dominated by radiation pressure on the Fe I atoms, as suggested by Brandeker (2011).

Most importantly, the temperature $\sim 1300 \text{ K}$ is found to be in striking agreement with the iron condensation temperature, which is of about 1350 K (Lodders 2003). This temperature could thus be considered as the sublimation temperature of grains, possibly drifting toward the star under the Poynting-Robertson effect, gas drag, or any other mechanism. Such grains can be produced by the evaporation of the exocomets that are regularly observed in the β Pictoris system (Kiefer et al. 2014), and can be the source of the Fe I seen in the stable circumstellar gas. In this scenario, the location of the observed Fe I atoms should be at the sublimation radius around the star, that is, at a distance of about $38 R_{\text{Star}}$ or $\sim 0.2 \text{ au}$ from the star, where the equilibrium temperature of grains is expected to be about 1350 K.

4.2. Physical conditions within the considered medium

In Fig. 8 we show all the Fe I excited levels, along with the 1300 K linear fit to the low-energy levels. If LTE conditions were met, the population of the medium- and high-energy levels would be distributed along that same line. This is obviously not the case, and as is shown by the vertical arrows, a jump is needed to reach the observed population. In agreement with Table 7, the radiation contribution to the equilibrium increases for groups on higher excitation levels. The higher the group, the larger the jump. As the contribution of radiation increases, the level distribution departs from a local linear distribution, showing evidence of non-LTE conditions for these groups.

However, we can still question the role of radiation in the low-energy level distribution.

4.2.1. Electronic volume density

One of the main effects of radiation is photoionization and thus the liberation of electrons in the surrounding medium. Measuring the electronic density will allow us to constrain the regime (collisional or radiative) of the medium at $38 R_{\star}$ from β Pictoris in Sect. 4.2.2. Lagrange et al. (1995) showed that the observed ratio $N(\text{FeI})/N(\text{FeII}) < 10^{-2}$, balanced by competing effects of radiation, collisions, and recombinations, requires the following condition at a distance r from the star: $4.5 \times 10^3 / r^2 > N_e \times T_e^{-0.89}$, where

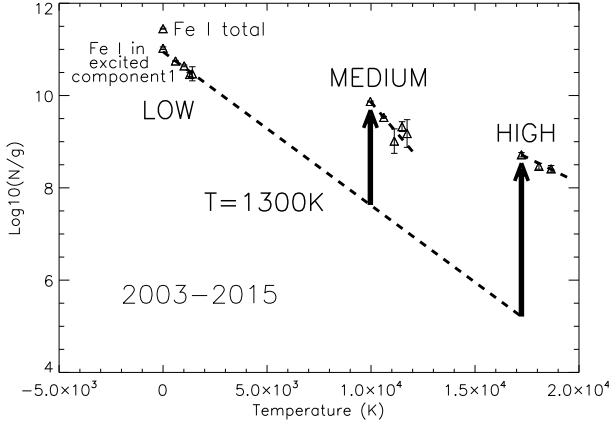


Fig. 8. Same as Fig. 6. The 1300 K thermodynamic equilibrium distribution corresponding to the lower energy levels is shown by a straight dashed line. The disagreement between this line and the observations related to the higher energy levels shows that indeed LTE is not reached for all levels. Table 7 explains at least qualitatively why such a situation is encountered, the two higher groups of energy levels are increasingly sensitive to radiation from the stellar photospheric flux, as shown by the two vertical jumps underlined by the two vertical arrows. Conversely, the lowest levels have five well-aligned levels and must be less sensitive to radiation and thus are mostly populated by another mechanism, likely collisions (see text).

N_e and T_e are the electronic density and temperature of the medium, and r is in AU. Applying this relation to a medium at 1300 K at 0.2 AU from the star, we find that $N_e < 6.7 \times 10^7 \text{ cm}^{-3}$. However, the Fe I lines are within a narrow spectral domain at about 20.4 km/s, while the Fe II absorption is observed at about 22 km/s (Lagrange et al. 1995); the $N(\text{FeI})/N(\text{FeII})$ ratio should hence be estimated using the column density of Fe II at 20.4 km/s (or 20.9 km/s when we take into account the 0.5 km/s shift between Fe II and Fe I; Brandeker et al. 2011). Lagrange et al. (1995) also evaluated the FWHM of Mn II and Zn II, which are 5.6 and 5.5 km/s, respectively. Thus only a small overlap exists between the 20.4 km/s spectral position and the blue edge of the Fe II line. This leads to a rough estimate of the Fe II column density in the same component as in Fe I of about 10^{-2} times the total column density measured by Lagrange et al. (1995). The column density ratio is thus more likely $N(\text{FeI})/N(\text{FeII}) \lesssim 1$, which yields an upper limit for the electronic density of $N_e \lesssim 7 \times 10^5 \text{ cm}^{-3}$. Combined with the condition given by Kondo & Bruhweiler (1985) that $N_e \geq 10^3 \text{ cm}^{-3}$ to explain the presence of excited levels of C I and Fe I, we find that the electron density should be

$$10^3 \text{ cm}^{-3} \leq N_e \lesssim 7 \times 10^5 \text{ cm}^{-3}$$

4.2.2. Possible equilibrium regimes

Following Viotti (1976), three possible regimes could be observed in a stellar vicinity: collisional, radiative and nebular.

Viotti (1976) showed in particular that these three regimes could be visualized in a $[W, N_e T_e^{1/2}]$ diagram, where

W is the dilution factor that measures the density of the stellar radiation in the stellar environment, and $N_e T_e^{1/2}$ represents the rate of electron impacts.

With $W = 1/2\{1 - [1 - (R_{\text{Star}}/R)^2]^{1/2}\}$, we can evaluate that the dilution factor at $R = 38 \times R_{\text{Star}}$ is $\log W = -3.76$. With the previous constraints found on N_e and assuming $T_e = 1300 \text{ K}$, we should have $1.44 \leq \log N_e T_e^{1/2} < 4.27$.

The $[W, N_e T_e^{1/2}]$ diagram (Viotti 1976 ; Fig 2) shows that the evaluated conditions locate the considered β Pictoris circumstellar medium in the radiative regime. However, Viotti (1976) computed his diagram for Be stars, which are more energetic in the UV than β Pictoris, and indicated in the diagram the positions of one more UV-energetic nova as well as the conditions in the photosphere of less UV energetic B-type stars (dwarf, BV, and supergiants, BI). We conclude that in the environment of less UV-energetic stars like β Pictoris (an A5V star), the position is shifted toward the right part of the diagram. This would place the medium of the observed excited Fe I lines in the radiative to collisional transition region, which is consistent with our evaluation from the excitation diagrams (see Fig. 8).

5. Conclusion

The present study of the large set of spectra of β Pictoris obtained with the HARPS instrument allowed a detailed analysis of the characteristics of the Fe I component and deriving a possible scenario for the origin of Fe I atoms observed in the “stable” circumstellar gas disk.

The main conclusions are listed below.

- Fe I is detected from the ground base level up to the 12969 cm^{-1} energy level.
- Fe I from the ground state is seen to be present within two components, one at 20.07 km/s and the other at 20.41 km/s radial velocity. The component at the lowest radial velocity is blueshifted relative to the main circumstellar gas; this blueshift gas can be dragged away by radiation pressure, as suggested by Brandeker (2011).
- The component at 20.41 km/s is common to all Fe I excited states. This component can be directly linked to source of Fe I atoms.
- The distributions of the low-energy levels are aligned in the excitation diagram and correspond to a temperature of about $\sim 1300 \text{ K}$ for the gas in the 20.41 km/s component.
- This temperature is similar to the Fe I sublimation temperature. We therefore conclude that the source of iron atoms in the inner circumstellar disk may be the evaporation of dust grains at about 0.2 AU or $38 R_{\text{Star}}$ from the stellar surface.

Although a complete non-LTE study needs to be made over the whole set of the excited Fe I level populations to completely identify the physical conditions in the medium, following Viotti (1976), we showed that the medium is likely in a transition regime between a radiative and a collisional regime. Further modeling is needed to confirm these preliminary evaluations.

Acknowledgements. We warmly thank F. Bouchy and the HARPS team for fruitful discussions on the subject of the present article.

Support for this work was provided by the CNES. We acknowledge the support of the French Agence Nationale de la Recherche (ANR), under program ANR-12-BS05-0012 Exo-Atmos. VB and DE acknowledge the financial support of the SNSF.

References

- Begelman, M. C. & Rees, M. J. 1976, *Nature*, 261, 298
- Beust, H., Lagrange-Henri, A. M., Vidal-Madjar, A., & Ferlet, R. 1989, *A&A*, 223, 304
- Beust, H., Vidal-Madjar, A., Ferlet, R., & Lagrange-Henri, A. M. 1990, *A&A*, 236, 202
- Beust, H., & Valiron, A. 2007, *A&A*, 466, 201
- Brandeker, A., Liseau, R., Olofsson, G., & Fridlund, M. 2004, *A&A*, 413, 681
- Brandeker, A. 2011, *ApJ*, 729, 122
- Dent, W. R. F., Wyatt, M. C., Roberge, A. et al. 2014, *Science*, 343, 1490
- Ehrenreich, D., Tinetti, G., Lecavelier des Etangs, A., Vidal-Madjar, A., & Selsis, F. 2006, *A&A*, 448, 379
- Ehrenreich, D., Hébrard, G., Lecavelier des Etangs, A., et al. 2007, *ApJ(Letters)*, 668, L179
- Ferlet, R., Vidal-Madjar, A., & Hobbs, L. M. 1987, *A&A*, 185, 267
- Fernández, R., Brandeker, A., & Wu, Y. 2006, *ApJ*, 643, 509
- Freistetter, F., Krivov, A. V., Löhne, T. 2007, *A&A*, 466, 389
- Genda, H. & Ikoma, M. 2008, *Icarus*, 194, 42
- Gry, C. & Jenkins, E. B. 2014, *A&A*, 567, 58
- Hébrard, G., Lemoine, M., Vidal-Madjar, A., et al. 2002, *ApJS*, 140, 103
- Hoyle, F. & Lyttleton, R. A. 1939, *Proc. Camb. Phil. Soc.*, 35, 405
- Hunten, D. M., Pepin, R. O. & Walker, J. C. G. 1987, *Icarus*, 69, 532
- Jolly, A., McPhate, J.B., Lecavelier des Etangs, A., et al. 1998, *A&A*, 329, 1028
- Kasting, J. F. & Pollack, J. B. 1983, *Icarus*, 53, 479
- Kiefer, F., Lecavelier des Etangs, A., Boissier, J., et al. 2014, *Nature*, 514, 462
- Kondo, Y., & Bruhweiler, F. C. 1985, *ApJ*, 291, L1
- Kral, Q., Wyatt, M., Carswell, R. F., Pringle, J. E., Matrà, L. & Juhász, A. 2016, *MNRAS*, in press, (arXiv:1606.01247)
- Lagrange, A.-M., Beust, H., Mouillet, D., et al. 1998, *A&A*, 330, 1091
- Lagrange, A.-M., De Bondt, K., Meunier, et al. 2012, *A&A*, 542, A18
- Lallement, R., Welsh, B. Y., Vergely, J. L., Crifo, F. & Sfeir, D. 2003, *A&A*, 411, L447
- Laviolette, P. A. 1987, *Earth Moon & Planets*, 37, 241
- Lecavelier des Etangs, A., Vidal-Madjar, A. & ferlet, R. 1996, *A&A*, 307, 542L
- Lecavelier des Etangs, A. 1998, *A&A*, 337, 501
- Lemoine, M., Vidal-Madjar, A., Hébrard, G., et al. 2002, *ApJS*, 140, 67
- Li, L. 2008 Nanjing Gamma-ray Burst Conference. AIP Conference Proceedings, 2008, 1065, 273
- Lodders, K. 2003, *ApJ*, 1220, 591
- Matrà, L., Dent, W. R. F., Wyatt, M. C. et al. 2017, *MNRAS*, in press, (arXiv:1609.06718)
- Mayor, M., Pepe, F., Queloz, D., et al. 2003, *The Messenger*, 114, 20
- McCrea, W. H. 1975, *Nature*, 255, 607
- Morbidelli, A., Chambers, J., Lunine, J. I., Petit, J. M., Robert, F., Valsecchi, G. B. & Cyr, K. E. 2000, *Meteorit. Planet. Sci.*, 35, 1309
- Pavlov, V. A. & Klabunovskii, E. I. 2015, *Russian Chemical Reviews*, 84, 121
- Pepe, F., Lovis, C., Ségransan, D., et al. 2011, *A&A*, 534, 58
- Pepin, R. O. 1991, *Icarus*, 92, 2
- Rampino, M. R. & Stothers, R. B. 1984, *Nature*, 308, 709
- Raymond, S. N., Quinn, T. & Lunine, J. I. 2004, *Icarus*, 168, 1
- Roberge, A., Feldman, P. D., Lagrange, A. M., Vidal-Madjar, A., Ferlet, R., Jolly, A., Lemaire, J. L. & Rostas, F. 2000, *ApJ*, 538, 904
- Roberge, A., Feldman, P. D., Weinberger, A. J., Deleuil, M. & Bouret, J.-C. 2006, *Nature*, 441, 724
- Rubenstein, E., Bonner, W. A., Noyes, H. P. & Brown, G. S. 1983, *Nature*, 306, 118
- Sekiya, M., Nakazawa, K. & Hayashi, C. 1980, *Prog. Theor. Phys.*, 64, 1968
- Slater, J. C. 1964, *Journal of Chemical Physics*, 41, 3199
- Smith, B. A. & Terrile, R. J. 1984, *Science*, 226, 1421
- Talbot, R. J., Jr. & Newman, M. J. 1977, *ApJS*, 34, 295
- Teiser, J. & Wurm, G. 2009, *MNRAS*, 393, 1584
- Trimble, V. 1983, *Rev. Mod. Phys.*, 55, 511
- Vidal-Madjar, A., Laurent, C., Bruston, P. & Audouze, J. 1978, *ApJ*, 223, 589
- Vidal-Madjar, A., Lagrange-Henri, A.-M., Feldman, P. D., et al. 1994, *A&A*, 290, 245
- Vidal-Madjar, A., Lecavelier des Etangs, A., & Ferlet, R. 1998, *Planet. Space Sci.*, 46, 629
- Viotti, R. 1976, *ApJ*, 204, 293
- Watson, A. J., Donahue, T. M. & Walker, J. C. G. 1981, *Icarus*, 48, 150
- Welsh, B. Y., & Montgomery, S. L., 2015, *Advances in Astronomy*, Volume 2015, Article ID 980323, 20 pages, <http://dx.doi.org/10.1155/2015/980323>
- Welsh, B. Y., & Montgomery, S. L., 2016, *PASP*, 128, 064201
- Zahnle, K. J., Kasting, J. F. & Pollack, J. B. 1988, *Icarus*, 74, 62